Semi-automatic aortic endograft localisation for post-operative evaluation of endovascular aneurysm treatment

Marleen de Bruijne, Wiro J. Niessen, J.B. Antoine Maintz, Max A. Viergever

Image Sciences Institute, University Medical Center Utrecht, The Netherlands

ABSTRACT

A semi-automatic method for localisation and segmentation of bifurcated aortic endografts in CTA images is presented. The graft position is established through detection of radiopaque markers sewn on the outside of the graft. The user indicates the first and the last marker, whereupon the rest of the markers are detected automatically by second order scaled derivative analysis combined with prior knowledge of graft shape and marker configuration. The marker centres obtained approximate the graft sides and central axis. The graft boundary is determined, either in the original CT slices or in reformatted slices orthogonal to the local graft axis, by maximizing the local gradient in the radial direction along a deformable contour passing through both sides.

The method has been applied to ten CTA images. In all cases, an adequate segmentation is obtained. Compared to manual segmentations an average similarity (i.e. relative volume of overlap) of 0.93 ± 0.02 for the graft body and 0.84 ± 0.05 for the limbs is found.

Keywords: marker detection, segmentation, boundary detection, dynamic programming, CTA, AAA, endovascular surgery

1. INTRODUCTION

An abdominal aortic aneurysm (AAA) is an enlargement of the infrarenal abdominal aorta, resulting from weakened arterial walls. Once present, AAAs continue to enlarge and, if left untreated, become increasingly susceptible to rupture, usually resulting in death. In conventional AAA treatment, the diseased part of the vessel is replaced by a synthetic graft during open surgery. This extremely invasive procedure has serious drawbacks including high mortality and complication rates and long hospital stays. Transfemoral endovascular aneurysm management (TEAM) is the minimally invasive alternative for AAA treatment[1]. Under fluoroscopic guidance an endograft is navigated through a small groin incision into the aorta, whereupon an attachment system consisting of a series of metal hooks is pressed into the vessel wall by means of balloon inflations. Despite initial success of this procedure, complications can arise in due course. The process of aneurysm shrinkage, ongoing aneurysmal disease, and damage or fatigue of graft material may result in leakage, graft migration, and kinking or buckling of the graft, which can subsequently cause rupture or occlusion.

Frequent and careful patient follow-up is therefore required[2,3]. In our study, Computer Tomographic Angiography (CTA) scans are made of each patient that has received an endograft, within 3 days after surgery. Follow-up scans are made every 3, 6 or 12 months, depending on the state of the aneurysm and the time elapsed since graft placement. In case of endoleak or other complications, intermediate scans may be taken every 1.5 months. The standard follow-up procedure includes definition of the central lumen line, enabling accurate graft and aneurysm diameter measurements, and graft lumen segmentation for graft volume measurement[4]. A volume representation of the graft enables clear visualization of graft morphology, thus revealing e.g. graft kinking or lengthening. Current practice in graft segmentation is thresholded 3D volume growing under expert supervision, in which the expert places seed points in the aorta and iliac arteries. All slices must be inspected; additional seed points can be placed in falsely excluded area's, and spurious regions, often caused by calcification or radiopaque markers, must be manually separated from the lumen in each slice. The central lumen line is established by positioning points in the centre of the lumen in all three orthogonal views of a multi-planar reformat facility. Both procedures are laborious and liable to inter- and intra-operator variations.

To our best knowledge, no previous research has concentrated on automated segmentation of aortic endografts. The problem is principally similar to the segmentation of pre-operative AAA[5,6], or more general, blood vessel

Further author information: M.B.: E-mail: M.deBruijne@azu.nl

segmentation, with graft metal induced bright streak artefacts and shadows as an additional difficulty. Juhan et al.[6] proposed a geometric modelling scheme that allows for extraction of the bifurcation and iliac arteries, but needs pre-processing in the form of supervised contour definition in each slice. Fiebich et al.[5] reported successful automated volume growing segmentation of the aorta and its branching vessels, but do not address the more difficult problem of segmenting the aortic bifurcation and the tortuous iliac arteries. In general, methods relying on 3D volume growing would encounter the same problems as our current expert guided segmentation in the presence of radiopaque markers. Another class of vessel segmentation methods uses multiscale higher order derivative analysis to determine the vessel central axis and boundaries[7,8]. These methods are able to cope with the varying width of the vessel but yield unreliable results in case of image artefacts, since the underlying assumption of the vessel shape does not hold.

Wink et al.[9] describe an automated central vessel axis extraction plus vessel border estimate. Given an approximation of the vessel axis, Verdonck et al.[10] established the lumen boundary through dynamic programming in reformatted slices perpendicular to that axis. These methods seem to be most robust in the presence of marker-induced artefacts, but cannot readily handle bifurcated vessels.

In this paper, a scheme for localisation and segmentation of the graft, based on automated detection of its radiopaque markers, is presented. The central axis and approximate boundary location can be deduced from the markers, and the rest of the boundary is determined through contour cost minimisation using dynamic programming. Once the marker locations are known, their artefacts can be accounted for.
Section 2 discusses the basic method for marker detection, graft localisation and graft segmentation. The results of the method as applied to ten CTA scans are presented in Section 3. Conclusions and suggestions for future work are given in Section 4.

2. DESCRIPTION OF THE METHOD

The graft segmentation procedure is preceded by a localisation step using the automated detection of the radiopaque markers that are sewn to the graft. Section 2.1 explains the layout of the graft, the marker configuration and the position in the image. The following sections describe the full segmentation process.

2.1. Description of the graft

Figure 1 shows the marker configuration on an EndoVascular Technologies (EVT) bifurcated aortic endograft, the type of aortic endograft that is used in the University Medical Center Utrecht. The markers on this graft are hollow platinum cylinders with a radius of 1 mm and length ranging from 1.5 to 5 mm. In CT images, they appear as bright elongated structures. Markers are sewn along the length of the graft 180 degrees apart, at intervals of approximately 10 mm. Only between the last two markers on the contra-lateral graft limb the distance is less than 5 mm instead of 10. The markers on the graft body are 3 mm in length on the ipsi-lateral (delivery catheter access) side and 1.5 mm on the contra-lateral side, aligned parallel to the graft axis. Two additional 3 mm markers are placed at the bifurcation. The markers on the limbs are 5 mm long and aligned perpendicular to the limb axis. The number of markers varies with the graft length. Available graft lengths are 12 to 19 cm, with 1 cm increments. The diameter varies from 20 to 26 mm.

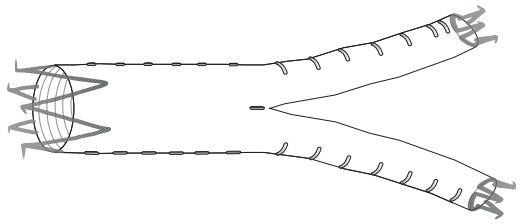

Figure 1. Scheme of a bifurcated endograft, showing marker configuration. Markers are sewn along the length of the graft 180 degrees apart. Two additional markers are placed in the bifurcation.

After graft placement the shape of the graft and its surrounding tissue can change considerably. The aneurysm sac generally shrinks when the pressure is released, as a consequence of which for instance calcifications that are distant from the lumen wall in the post-operative scans may be near the graft in a follow-up scan. In many patients,

kinking or buckling of the graft has been observed[3]. An example of observed morphologic changes after the procedure is given in Figure 2.

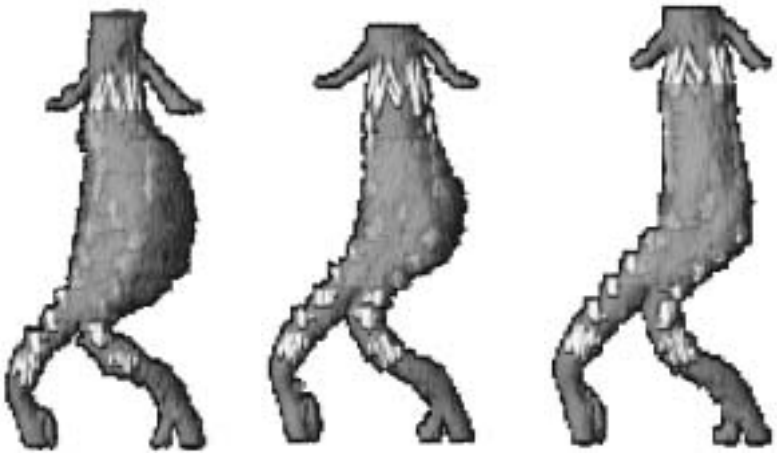

Figure 2. Volume representations of the graft and aneurysm in one patient, post-operative (left), after 1 year (middle), and after 4 years (right).

2.2. Marker detection

The markers are enhanced by means of a second order derivative filter based on the eigenvalues of the Hessian matrix H^{11} at a given voxel x. $H(\mathrm{x})$ describes the local second-order structure in the original grey-valued image $L(\mathrm{x})$

$$H(\mathrm{x}) = \begin{pmatrix} L_{xx}(\mathrm{x}) & L_{xy}(\mathrm{x}) & L_{xz}(\mathrm{x}) \\ L_{yx}(\mathrm{x}) & L_{yy}(\mathrm{x}) & L_{yz}(\mathrm{x}) \\ L_{zx}(\mathrm{x}) & L_{zy}(\mathrm{x}) & L_{zz}(\mathrm{x}) \end{pmatrix} \tag{1}$$

where subscripts denote derivatives to the corresponding spatial variables. Derivatives are computed by convolution with the derivative of a Gaussian kernel at scale σ

$$L_{ij} = L \star \frac{\partial^2}{\partial i \partial j} G(\mathrm{x}, \sigma) \tag{2}$$

$$i, j \in \{x, y, z\}$$

$$G(\mathrm{x}, \sigma) = \frac{1}{\sqrt{2\pi\sigma^2}^3} e^{-\frac{||\mathrm{x}^2||}{2\sigma^2}}. \tag{3}$$

We denote the eigenvalues of $H(\mathrm{x})$ by λ_1, λ_2, and λ_3, such that $|\lambda_1| \geq |\lambda_2| \geq |\lambda_3|$. Then, λ_1 represents the maximum local isophote curvature, and λ_3 the minimum.

Since the markers are bright and elongated in one direction, the local second order structure at a marker voxel will reveal a strong negative curvature in the directions perpendicular to the marker axis, and a weaker, but still negative, curvature in the parallel direction. In terms of eigenvalues this means $\lambda_1 \approx \lambda_2 < \lambda_3 < 0$. At small scales, the parallel curvature, λ_3, decreases from the marker ends towards the centre. However, at sufficiently large scales the output of both endpoints will coincide at the centre. Thus, at appropriate scales, the marker centre is associated with a local minimum in the product of the eigenvalues of the Hessian matrix.

A feature image containing the product of the eigenvalues of H at each voxel is computed. In this image, local minima that are formed by three negative eigenvalues correspond to the centres of bright blob-like structures in the original image and are potential marker centres. Local minima are detected by comparing the grey-values in a 3×3 -neighborhood for each voxel. A voxel is a local minimum if all of its 26 neighbours have higher grey-values. If at least one of the neighbours has equal grey-value and none is lower, the cluster of connected voxels with equal

grey-value forms a local minimum, from which we select the centre of gravity as the absolute local minimum. All local minima thus detected are stored as potential marker centres, the product of eigenvalues representing their marker likeness.

2.3. Marker selection

The set of potential marker coordinates resulting from the marker detection procedure not only contains all markers, but also a number of false positives induced by other structures that are similar to the markers in size, shape and grey-value. Additional information is needed to discern the true markers from other marker-resembling structures and to determine the proper ordering of markers along the graft. For this purpose, prior knowledge on marker configuration and possible graft shapes can be used.

We should be able to distinguish the true markers among marker-like structures on basis of their relative position in the image. To gain insight in post-operative graft morphology, the marker configuration is examined in datasets where all markers have been indicated manually. Since the automated procedure will have to cope with a relatively large deviation in graft postures and variations in the surrounding tissue, a diverse set of images is used, containing ten CTA scans taken from different patients 0 to 48 months after graft placement, with graft lengths varying from 13 to 19 cm, and including kinked and rotated grafts and patients with endoleak.

The occurring distances between successive markers, the distance from the most proximal markers to the bifurcation markers, and the angles between the lines connecting each marker with its predecessor and its successor were measured. These characteristics are different for the proximal and the distal part of the graft. The graft body is generally straighter than the limbs, which extend into the often tortuous iliaca. Furthermore, a large gap can exist between the proximal and distal markers. The distances and angles measured are shown in Figure 3.

From Figure 3 we learn that, for example, in the graft limbs in our data sets the region in which the next marker can be positioned is described by the part of a sphere, bounded by 3 and 15 mm, and making an angle of up to 125 degrees with the vector connecting this marker to its predecessor. However, this region might also comprise two or more successive markers. To handle all occurring cases, an iterative approach is chosen. First, the marker is sought for in a small search space. If no marker is found, the search space is enlarged. The boundaries of the search spaces are shown as rectangular regions in Figure 3. The initial search space size is set such that the average distance or angle plus one standard deviation are enclosed, unless the chance of having two markers in that region would be large, in which case the first distance bound is kept smaller. The other search spaces comprise roughly 80%, 90%, and 100% of the markers. In this way, the chance of skipping one marker in the first search space is minimised, while outliers can be captured in the largest.

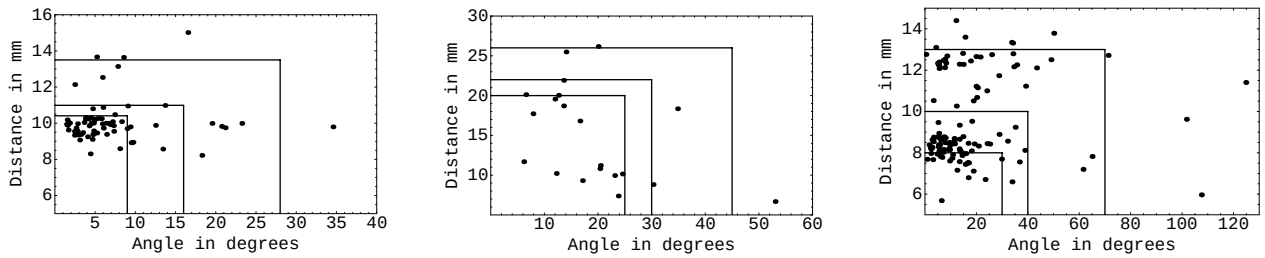

Figure 3. Distances between successive markers and angles between line segments connecting successive markers, as measured in the graft body (left), in the limbs (right), and in between (middle).

Given the marker candidates detected in Section 2.2 and the search spaces as defined above, the following algorithm was employed to track a series of successive markers on either side of the graft. The operator initialises the graft localisation process by indicating the four markers at the proximal and distal ends of the graft. The marker candidates that are nearest to the indicated points are selected as the end markers. Subsequently, the bifurcation markers are searched for automatically at distances between 30 and 80 mm down from the proximal markers. The bifurcation markers can be discriminated from other pairs of markers or other bright structures since they are closer to each other than the other markers, distances of 4.5 to 7.5 mm have been observed. Moreover, they are of the same size and therefore will have similar marker likeness.

Once the bifurcation markers have been found, successive markers are recursively searched from all four user-indicated markers. Tracing down from the proximal end markers and up from the distal end markers, the strongest marker candidate in the smallest search space is selected. If no suitable marker candidate was found, the process is repeated with a larger search space. When a successor is found, the tracking continues from that marker along the direction from the previous marker to the current one. Beyond the bifurcation markers the search spaces adapt to the different expected distance and angle in this part of the graft. If even the largest search space does not contain a suitable successor, but it does contain the bifurcation markers, the search space is adapted to close the gap between the proximal and distal part, and is subsequently adapted for the other (proximal or distal) part. Otherwise, the process stops and waits for the opposing line to grow near. If the process has stopped at both ends of one side, the searching is continued in the direction of the opposite end marker.

The algorithm terminates if no successors are found or the two lines on one side of the graft connect, i.e. when the end of the opposite line is encountered in the search space.

2.4. Graft segmentation

The locations of the markers confine the graft lumen and approximate the central lumen axis. In sequential two-dimensional cross-sections, the graft boundary is searched in a circular region comprising the approximate border location. Two approaches were tested: the first performs the graft contour detection in the original CT-slices, the second in reformatted slices orthogonal to the central axis.

2.4.1. Slice-based approach

Cubic spline interpolation between the markers defines two graft side points in each slice. The spatial average of those side points approximates the vessel centre for the proximal part of the graft.

Polar plots are constructed in each slice, showing the grey-values along lines departing from the centre point. The plots are bounded by a minimum radius r_1 and a maximum radius r_2. Given the in-slice voxel dimensions $d \times d$, the polar plot is interpolated such that the number of voxels in the radial direction n_r and in the tangential direction n_t are given by

$$n_r = \frac{r_2 - r_1}{d} \tag{4}$$

and

$$n_t = \frac{2\pi r_2}{d}. \tag{5}$$

The confining radii r_1 and r_2 are defined by R, the obtained distance from the centre to the graft side, and a tuneable parameter that allows for deviations from circular shape as well as some inaccuracy in the side point detection:

$$r_1 = R - s_1 \tag{6}$$

$$r_2 = R + s_2. \tag{7}$$

The parameters s_1 and s_2 should be as small as possible, but large enough to ensure that the full graft boundary is included always. Figure 4 illustrates the importance of search space confinement. In this slice, the lumen border is determined correctly, but if the allowed radius is larger part of the thrombus boundary is traced instead. In all our experiments s_1 and s_2 are fixed at 4 mm and 1 mm respectively. s_2 Can be smaller than s_1 because if the graft cross-section is stretched to an elliptical shape, the axis connecting the markers is generally the major axis. In the graft limbs, the expected radius is half the proximal radius, but the centre estimate is less accurate and there is no preferred direction for the deviation from a circular shape. Both s_1 and s_2 are then set to 4 mm.

In the thus constructed polar plot the edges in the tangential direction (t) are enhanced through convolution with the 2-dimensional scaled Gaussian derivative in radial direction (r):

$$L_{rt} = L \star \frac{\partial}{\partial r} G(\mathrm{x}, \sigma) \tag{8}$$

$$G(\mathrm{x}, \sigma) = \frac{1}{2\pi\sigma^2} e^{-\frac{||\mathrm{x}^2||}{2\sigma^2}}. \tag{9}$$

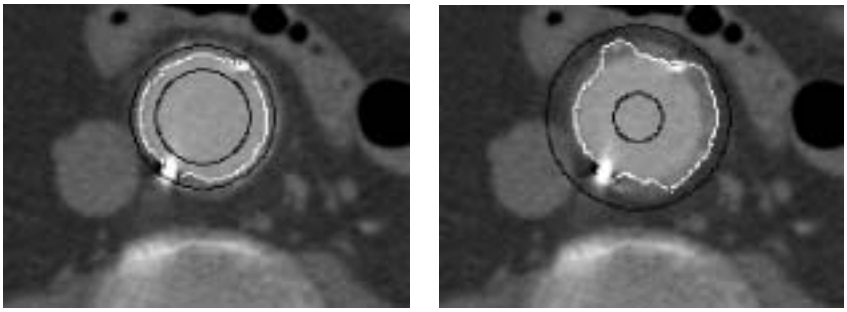

Figure 4. Example CTA slice showing the boundaries of the polar plot (black) and the contours detected (white). If the region in which the contour is searched is taken larger, part of the thrombus boundary is included in the detected optimal path.

The scale σ is kept small (1 mm) to obtain the most detailed edge information. As the lumen is bright on a darker background, the lumen wall corresponds with a local minimum in the radial gradient. The optimal path through both established side points and covering minimal radial gradient is obtained through dynamic programming.

With respect to the graft cross-sectional shape we can distinguish three stages. While the contour of the graft starts out as a circular or oval shape near the proximal attachment, approaching the bifurcation it gradually becomes more '8-shaped'. Then, we can no longer assume that the graft boundary has minimal gradient in the radial direction at any point. We overcome this problem by searching for two smaller intersecting circles instead of one. To keep the search space as large as needed, but as small as possible, the maximum radius of these two 'circles' is larger towards the centre of the graft than towards the outside. Beyond the bifurcation, for each limb only one side can be deduced from the markers, and the lumen centre is estimated from the adjacent contour. Figure 5 shows an example of the confined search region and the detected contour for each part of the graft.

A voxel representation of the graft lumen is constructed by flood filling the obtained contours.

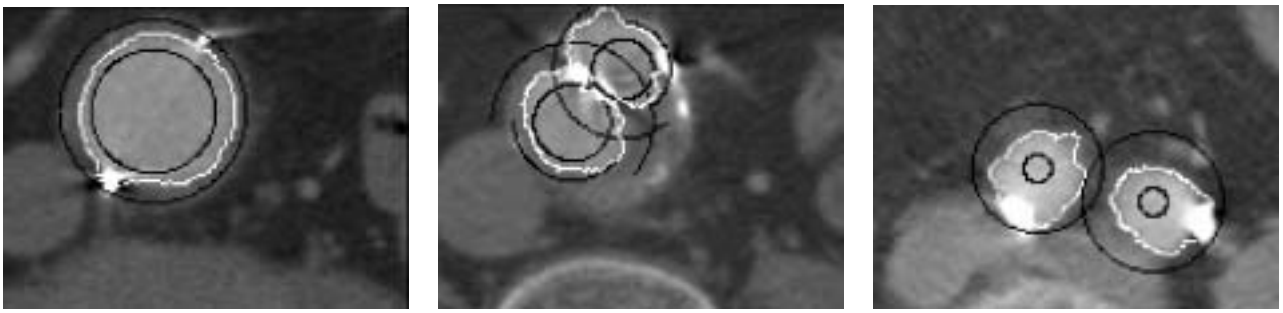

Figure 5. Example CTA slices showing the boundaries of the polar plot (black) and the contours detected (white) for, from left to right: the proximal part of the graft; just above the bifurcation; and the distal graft part.

2.4.2. Orthogonal to the graft axis

The central vessel axis is established as in 2.4.1. It is then resampled such that there is a sample point in each voxel the spline passes through. For each sample point, a polar plot is constructed in the plane through the sample point and locally perpendicular to the axis. The plots are bounded, and the contours searched, in the same way as in the slice-based approach. Beyond the bifurcation, the centres are estimated from the adjacent contours, and the polar plots are constructed around the estimated centre point but perpendicular to the graft side. As the searched contours are approximately perpendicular to the limb axis, the deviation from a circle should be less than in the slice-based approach and the centre estimate should be more accurate. Therefore s_1 and s_2 are chosen smaller, both 2 mm.

The result is an ordered set of non-parallel contours. Construction of a voxel representation is less straightforward than in the slice-based approach. Since the established contours are close, satisfactory results can be obtained by

connecting adjacent contours with line segments such that continuous contours are generated in each slice. A slice can contain several intersecting contours, of which the outer envelope defines the graft wall and can be obtained through region growing of the background.

3. EXPERIMENTS AND RESULTS

The three stages of graft segmentation as described in Section 2, namely marker detection, marker selection, and two different approaches for graft boundary detection, are applied to ten CTA images from patients in 0 to 48 months follow-up. The scan resolution is $0.485 \times 0.485 \times 2.0$ mm. The images consist of circa 125 slices of 512×512 voxels. Each image contains between 20 and 32 markers, depending on the length of the implanted graft (ranging from 13 to 19 cm). In the ten images, a total of 266 markers is present.

3.1. Marker detection

The marker detection filter was applied at scales σ ranging from 1 to 8 mm. The resulting potential markers, sorted on basis of decreasing marker likeness, were compared to the outcome of a manual marker detection strategy in which an operator points out the centre of each marker in a multi-planar reformat facility. A marker candidate is considered a true marker if it lies within a 2-mm distance (the slice thickness) to one of the points indicated manually, and if that point has not yet been associated with another marker candidate. Otherwise, it is a false positive.

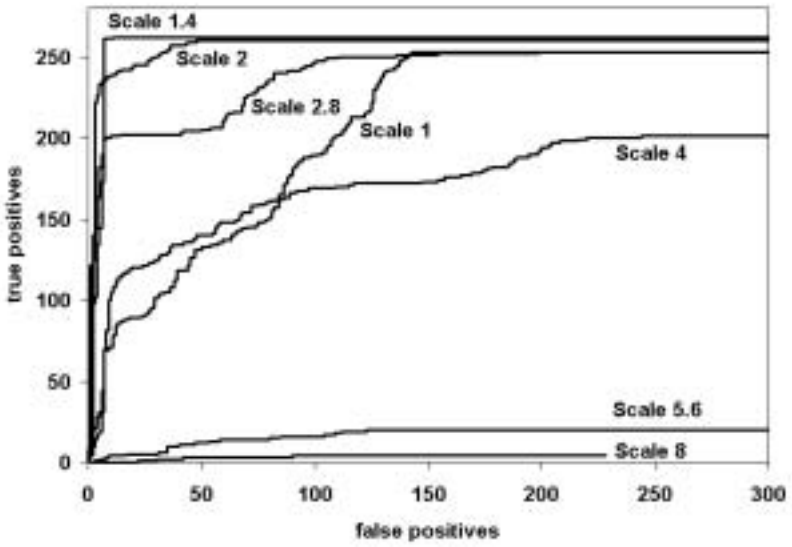

Figure 6. ROC curve of markers detected in ten images at scales ranging from 1 to 8 mm. The total number of markers present in the images is 266, the maximum number detected is 262.

Figure 6 shows the results for each scale, summed over all ten images, in a Receiver Operator Characteristic (ROC) curve. Sorted by decreasing marker likeness, the number of markers detected correctly is plotted as a function of the number of false positives. The area under a ROC curve measures the accuracy of the test, in this case its ability to distinguish between true markers and other bright blob-like structures present in the image. Clearly, the filter performs best at a scale of 1.4 mm, which is the size of the smallest markers. At smaller scales, many of the larger markers are detected as two separate smaller markers, of which one is counted as a false positive in our evaluation. At much larger scales, $\sigma \geq 4$ mm, two separate markers may be detected as one.

At the optimum scale of 1.4 mm, 262 out of the total of 266 markers were detected, and 6 false positives were found before the weakest marker. Three of the cases in which a marker was not detected were caused by the two contra-lateral end markers, which are very close and visually hard to distinguish, being detected as one. In the fourth case the marker was actually detected but at a distance of 2.3 mm from the manually indicated marker centre, slightly over the allowed 2 mm. These errors will not hamper the use of the marker configuration as an initialisation

for graft segmentation. The false positives are mainly owing to some of the larger distal markers being detected as two markers instead of one. Since the two markers detected are very close, selecting either one is acceptable, but for the continuity in the approximated side lines selecting both must be avoided.

The number of true positives remains steady at scales near the optimum scale. However, the number of false positives increases rapidly, which implies that additional information may be needed to distinguish all markers from other marker resembling structures appearing in a wider range of images. Furthermore, the graft configuration still needs to be established.

3.2. Marker selection

The marker selection scheme as described in 2.3 was applied to the set of marker candidates that have been detected at the optimum scale of 1.4 mm. In all cases, our algorithm was able to find the bifurcation markers and track series of markers on the side of the graft, without including other marker-like structures. In 7 out of 10 scans, all markers were found. When during marker detection the two end markers were detected as one, naturally only one marker could be selected. In two scans an additional marker was missed because two successive markers were both captured in one search space, and then only the strongest is selected. Nevertheless, the graft sides could still be properly estimated.

The exact positions indicated by the user are of negligible influence to the final graft approximation, provided that they are within a reasonably small distance, i.e. a few mm, to the true end marker position. As the marker candidate nearest to the indicated point is selected, even if that is not the intended end marker it should be either another marker, causing the segmentation to be only shorter, or a false positive. False positives are caused by marker resembling structures, which could in this case be either parts of the attachment system or calcification, which are also situated on the outside of the lumen and thus will not introduce a large error in the approximated graft side. In the ten scans of this study the proper end markers were always found.

3.3. Graft segmentation

One dataset could not be segmented using the slice-based approach since part of the graft was aligned in-plane, showing several successive markers in one slice. Segmenting orthogonal to the vessel axis was possible in this patient. Figure 7 shows volume representations for one patient, segmented by means of: (1) thresholded region growing under expert guidance, the current practice; (2) the proposed method, slice-based; and (3) the proposed method, orthogonal to axis.

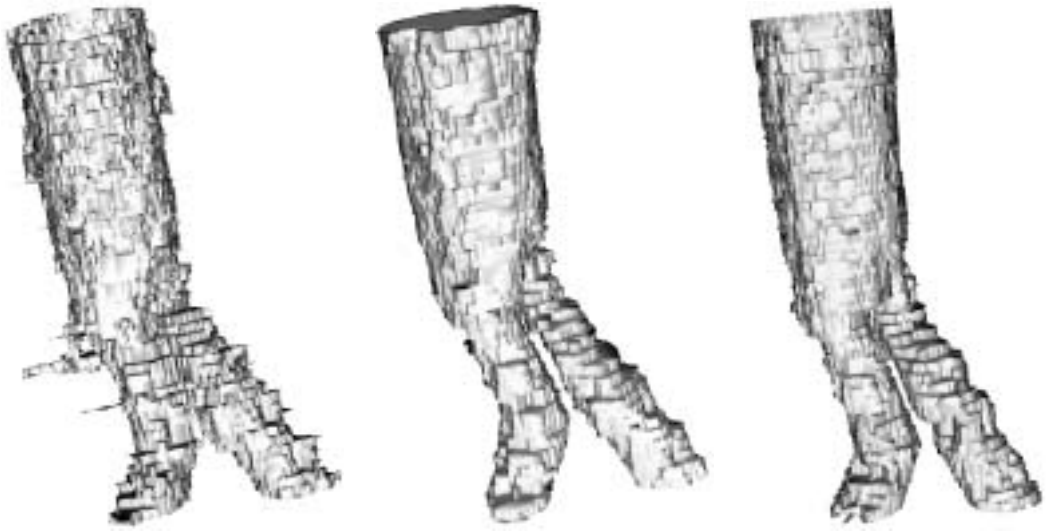

Figure 7. Volume representation of the graft of patient II, segmented by means of thresholded region growing under expert guidance (left), the slice-based approach (middle), and the approach orthogonal to the graft axis (right).

The segmentations obtained by our method are smoother than the expert segmentation, mainly owing to marker-induced bright streak artefacts that are included in the region growing process. Markers can also give rise to shadows in the lumen, causing holes in the volume obtained by region growing. In addition, we observe that both automated procedures measure two separate limbs, while the expert segmentation tends to combine the limbs into one region. Cross-sectional images of the limbs in the original CTA image and in the segmentations are shown in Figure 8. They reveal that the graft at that position does indeed consist of two separate lumens. Furthermore, the slice-based approach shows a slight undersegmentation of the graft limbs. This can be explained since the contour is searched in a circular region confined by the approximate limb radius, while the limbs are not parallel to the scan axis wherefore the in-slice contour will be elliptic instead of circular. Although the limb segmentation has improved in the orthogonal approach, large steps can still be seen, mainly because the orthogonal contours had to be transformed back to an anisotropic voxel representation to enable comparison with the other segmentations.

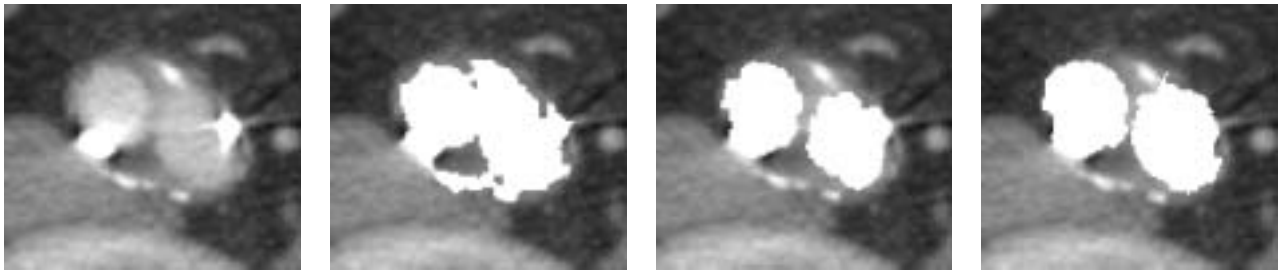

Figure 8. CTA slice of patient II (left), segmented by region growing under expert guidance (second), the slice-based approach (third) and the approach orthogonal to the graft axis (last).

The similarity, or relative volume of overlap, of two volumes A and B is defined by

$$2\,\frac{A \cap B}{A + B} \tag{10}$$

Table 1 lists the similarity of the automated and expert segmentations for each scan. The slice-based and the orthogonal approach yield similar results. The results for the graft body show good agreement with the expert segmentation; the average volume of overlap is 93±2%. The segmentations obtained for the graft limbs agree in a lesser extent, 84±5%. This may be caused by the merging of the limbs in the region growing process.

Table 1. Relative volume of overlap as compared to the expert segmentation

	Proximal		Distal	
Patient	slice-based	orthogonal	slice-based	orthogonal
I	0.95	0.94	0.73	0.77
II	0.93	0.94	0.76	0.81
III	0.93	0.88	0.75	0.86
IV	-	0.95	-	0.78
V	0.94	0.93	0.79	0.85
VI	0.93	0.93	0.88	0.88
VII	0.95	0.95	0.90	0.89
VIII	0.95	0.94	0.87	0.88
IX	0.93	0.92	0.92	0.89
X	0.94	0.93	0.84	0.80
Average	0.94 ± 0.01	0.93 ± 0.02	0.82 ± 0.07	0.84 ± 0.05

The relative difference in measured volume of B with respect to A, defined by

$$\frac{B-A}{A} \tag{11}$$

is given in Table 2, for the automated segmentations with respect to the expert segmentations. In Patient III, in particular for the graft body, we obtained a large oversegmentation of 13% using the slice-based approach and even 25% using the orthogonal approach. Closer investigation revealed thrombus development inside the proximal part of the graft in this patient, wherefore the lumen boundary lies within the graft and is not defined by the markers. Obviously, our method is not suited for segmenting these images. The error is easily recognized however, and the obtained segmentation can still be used for the parts of the graft that do not contain thrombus. When we ignore patient III the average volume differences for the graft body are -2±5% and 1±7% for the slice-based and the orthogonal approach respectively, and for the limbs -17±13% and -9±9%. The average absolute volume differences are 4±3%, 6±3% , 17±13% and 11±6%.

For the graft body, the slice-based and the orthogonal procedures both yield similar, good results. As was anticipated, both approaches show an undersegmentation of the graft limbs with respect to the expert segmentation, but the results of the orthogonal approach are better.

Table 2. Relative volume difference as compared to the expert segmentation (percentage).

	Proximal		Distal	
Patient	slice-based	orthogonal	slice-based	orthogonal
I	5.3	8.6	-37	-13
II	-10	-7.3	-34	-19
III	13	25	-30	2.0
IV	-	-5.9	-	-21
V	-3.7	-3.3	-8.7	3.3
VI	0.074	5.8	-7.5	-4.1
VII	-4.9	-0.28	-12	-8.9
VIII	1.1	4.0	-19	-8.9
IX	4.8	11	0.090	6.4
X	-5.5	-3.3	-16	-12
Average	0 ± 7	3 ± 10	-18 ± 13	-8 ± 9

To investigate the results in terms of differences in obtained contours, the morphologic dilation and erosion of the expert segmentation A are computed per slice, using a 3×3 square structuring element. The difference between the dilated and the eroded volume corresponds to twice the error volume for a contour diverging one voxel from the contour of A. Thus,

$$2\,\frac{A \cup B - A \cap B}{A_{Dilated} - A_{Eroded}} \tag{12}$$

gives the average deviation in voxels of the obtained contour with respect to the expert segmentation. This evaluation is slightly biased in favour of the slice-based approach, since then the comparing of contours is performed in the same slices as the contour detection itself. Both approaches obtain however similar results. Averaged over all ten datasets the contour deviation is circa one voxel for the graft body (0.45±0.05 mm and 0.49±0.07 mm for the slice-based and orthogonal approach respectively), and less than two voxels for the graft limbs (0.7±0.3 mm and 0.8±0.2 mm).

4. CONCLUSIONS AND FUTURE WORK

In this paper we presented a method to segment bifurcated aortic endografts in CTA scans with only a minor user initialisation. Two methods were tested, the first performed graft contour detection in the initial CT-slices, the other in reformatted slices orthogonal to the graft axis. For the proximal part of the graft, where the graft is still fairly

straight and parallel to the body axis, both methods yield similar results, in good agreement with the segmentations obtained by the expert. The average volume of overlap was 93±2%. Beyond the bifurcation the method depending on the original CT-slices shows a strong volume underestimation with respect to the expert measurements. This is anticipated as the underlying assumption that the graft contour is approximately circular does not hold when the lumen is oriented more parallel to the slice, which is often the case in the tortuous graft limbs. The results of the orthogonal approach are in better agreement with the expert segmentation but still reveal a slight underestimation (8±9%). This could be explained since the expert guided volume growing process tends to fuse the two graft limbs into one single region, thus obtaining an oversegmentation with respect to the true lumen.

Visual inspection of the obtained segmentations suggests that the automated method is not only labour reducing and free from intra-operator variations, but also yields clinically better segmentations, as prior knowledge of graft shape is employed to reduce the influence of markers, calcifications, and image artefacts. We must however bear in mind that the use of prior knowledge may decrease the ability to deal with anomalies in graft shape. This holds for this study in particular since we have used the same set of scans for both the investigation of post-operative marker configuration and the evaluation of the full segmentation procedure. A more extensive evaluation is needed to ensure our segmentations fulfil clinical requirements. We are currently validating the results and the value of the current 'gold standard', i.e. the expert segmentation.

Our method would be easily extended to cope with the other types of aortic endograft, viz. the tube graft and the mono-iliac graft. For this study we have chosen the bifurcated graft, since it is most commonly used and the most difficult to segment. Although the currently required user interaction is only small, the process may be fully automated in the future. Furthermore, we intend to investigate the benefit of an iterative boundary detection process, in which the distance between sequential contours can be taken into account in the cost minimisation. The following step will be the extension of the graft segmentation method described to address the problem of thrombus segmentation.

5. ACKNOWLEDGMENTS

This research was funded by the Netherlands Organization for Scientific Research (NWO).
Presentation at this conference was partially supported by a grant from the Whitaker Foundation.
We would like to thank Drs. M. Prinssen, Dr. I. Broeders, and Dr. J. D. Blankensteijn from the Department of Vascular Surgery for many useful discussions, and for providing the data sets and expert segmentations.

REFERENCES

1. J. C. Parodi, J. Palmaz, and H. Barone, "Transfemoral intraluminal graft implantation for abdominal aortic aneurysms," *Annals of Vascular Surgery* **5**, 1991.
2. I. A. M. J. Broeders, J. D. Blankensteijn, A. Gvakharia, J. May, P. R. F. Bell, J. Swedenborg, J. Collin, and B. C. Eikelboom, "The efficacy of transfemoral endovascular aneurysm management: A study on size changes of the abdominal aorta during mid term follow up," *European Journal of Vascular and Endovascular Surgery* **14**(2), pp. 84–90, 1997.
3. J. J. Wever, *CT Angiographic Follow-up after Endovascular Aortic Aneurysm repair.* PhD thesis, Utrecht University, 1999.
4. R. Balm, R. Kaatee, J. D. Blankensteijn, W. P. T. M. Mali, and B. C. Eikelboom, "CT-angiography of abdominal aortic aneurysms after transfemoral endovascular aneurysm management," *European Journal of Vascular and Endovascular Surgery* **12**(2), pp. 182–188, 1996.
5. M. Fiebich, M. T. Mitchell, R. M. Engelmann, and K. R. Hoffmann, "Automatic segmentation in CT angiography of the abdominal aorta," in *Computer Assisted Radiology and Surgery*, H. U. Lemke, M. W. Vannier, and K. Inamura, eds., pp. 277–282, Elsevier Publishers, Amsterdam, 1997.
6. V. Juhan, B. Nazarian, K. Malkani, R. Bulot, J. M. Bartoli, and J. Sequeira, "Geometrical modelling of abdominal aortic aneurysms," in *Proc. CVRMed and MRCAS*, No. 1205 in Lecture Notes in Computer Science, pp. 243–252, Springer Verlag, Berlin, 1997.
7. C. Lorenz, I. C. Carlsen, T. M. Buzug, C. Fassnacht, and J. Weese, "Multi-scale line segmentation with automatic estimation of width, contrast and tangential direction in 2D and 3D medical images," in *Proc. CVRMed and MRCAS*, No. 1205 in Lecture Notes in Computer Science, pp. 233–242, Springer Verlag, Berlin, 1997.

8. Y. Sato, S. Nakajima, N. Shiraga, H. Atsumi, S. Yoshida, T. Koller, G. Gerig, and R. Kikinis, "Three-dimensional multi-scale line filter for segmentation and visualization of curvilinear structures in medical images," *Medical Image Analysis* **2**(2), pp. 143–168, 1998.
9. O. Wink, W. J. Niessen, and M. A. Viergever, "Fast delineation an visualization of vessels in 3-D angiographic images," *IEEE Transactions on Medical Imaging* **19**(4), pp. 337–346, 2000.
10. B. Verdonck, I. Bloch, H. Maître, D. Vandermeulen, P. Suetens, and G. Marchal, "Accurate segmentation of blood vessels from 3D medical images," in *IEEE International Conference on Image Processing*, pp. 311–314, 1996.
11. T. Lindeberg, *Scale-Space Theory in Computer Vision*, Kluwer Academic Publishers, Dordrecht, the Netherlands, 1994.